

Cite this: *Energy Environ. Sci.*,  
2018, 11, 2235

## The balance of electric field and interfacial catalysis in promoting water dissociation in bipolar membranes†

Zhifei Yan,<sup>‡a</sup> Liang Zhu,<sup>‡b</sup> Yuguang C. Li,<sup>‡a</sup> Ryszard J. Wycisk,<sup>‡c</sup>  
Peter N. Pintauo,<sup>‡c</sup> Michael A. Hickner<sup>‡b</sup> and Thomas E. Mallouk<sup>‡\*a</sup>

The lamination of a cation exchange layer (CEL) and an anion exchange layer (AEL) to form a hybrid bipolar membrane (BPM) can have several unique advantages over conventional monopolar ion exchange membranes in (photo-)electrolysis. Upon application of a reverse bias, the ordinarily slow water dissociation reaction at the AEL/CEL junction of the BPM is dramatically accelerated by the large electric field at the interface and by the presence of catalyst in the junction. Using electrochemical impedance spectroscopy (EIS), we have found a counterbalanced role of the electric field and the junction catalyst in accelerating water dissociation in a BPM. Experimental BPMs were prepared from a crosslinked AEL and a Nafion CEL, with a graphite oxide (GO) catalyst deposited at the junction using layer-by-layer (LBL) assembly. BPMs with an interfacial catalyst layer were found to have smaller electric fields at the interface compared to samples with no added catalyst. A comprehensive numerical simulation model showed that the damping of the electric field in BPMs with a catalyst layer is a result of a higher water dissociation product ( $\text{H}^+/\text{OH}^-$ ) flux, which neutralizes the net charge density of the CEL and AEL. This conclusion is further substantiated by EIS studies of a high-performance 3D junction BPM that shows a low electric field due to the facile catalytic generation and transport of  $\text{H}^+$  and  $\text{OH}^-$ . Numerical modeling of these effects in the BPM provides a prescription for designing membranes that function at lower overpotential. The potential drop across the synthetic BPM was lower than that of a commercial BPM by more than 200 mV at  $>100 \text{ mA cm}^{-2}$  reverse bias current density, with the two membranes having similar long-term stability.

Received 22nd April 2018,  
Accepted 1st June 2018

DOI: 10.1039/c8ee01192c

rsc.li/ees

### Broader context

Bipolar membranes (BPMs) have recently been shown to offer important advantages over conventional monopolar membranes in avoiding polarization losses in (photo-)electrochemical water splitting and carbon dioxide reduction. The rate of water dissociation at the junction between the cation and anion exchange layers (CEL and AEL) limits the energy efficiency of BPM-based electrolysis devices. This rate is dramatically increased by the high electric field and the presence of catalysts in the junction region. Realizing high performance BPMs requires knowledge of the relative importance of and correlation between the electric field and the catalyst in promoting water dissociation. Here a combined electrochemical impedance and simulation study reveals that the electric field across the AEL/CEL interface is weakened by the  $\text{H}^+/\text{OH}^-$  flux from catalyzed water dissociation, which partially neutralizes the unbalanced fixed charges on the AEL and CEL. The understanding gained from this study highlights the need to optimize the amount of catalyst in the AEL/CEL junction, as found empirically in previous studies, and offers some basic principles for designing higher performance BPMs.

### Introduction

Much of current (photo-)electrolysis research focuses on developing efficient and cost-effective catalysts to lower the over-potential for water splitting<sup>1–5</sup> and  $\text{CO}_2$  reduction.<sup>6–15</sup> Relatively little attention has been paid to mass transfer management of reactants, ions and products, the understanding of which is essential for a robust and stable electrolysis system.<sup>16–18</sup> Proton transport, in particular, is a vital process in an electrolysis cell because cathodic electron transfer

<sup>a</sup> Departments of Chemistry, Biochemistry and Molecular Biology, and Physics, The Pennsylvania State University, University Park, Pennsylvania 16802, USA.  
E-mail: tem5@psu.edu

<sup>b</sup> Department of Materials Science and Engineering, The Pennsylvania State University, University Park, Pennsylvania 16802, USA

<sup>c</sup> Department of Chemical and Biomolecular Engineering, Vanderbilt University, Nashville, TN 37235, USA

† Electronic supplementary information (ESI) available. See DOI: 10.1039/c8ee01192c

‡ These authors contributed equally to this work.

is accompanied by the consumption of protons, for example in the hydrogen evolution reaction (HER) and in CO<sub>2</sub> reduction.<sup>7,19</sup> Membrane separators are typically incorporated into the electrolysis system to allow for selective passage of electrolyte ions and the separation of the cathodic and anodic products.<sup>17,20</sup> Mass transfer in membrane separators can induce additional resistance and can result in a transmembrane pH gradient, compromising the energy efficiency of the system.<sup>21–23</sup> Although commercial electrolyzers normally operate under strongly acidic or basic conditions to minimize series resistance,<sup>24</sup> pH neutral electrolytes are advantageous for some oxygen evolution reaction (OER) catalysts that contain only earth-abundant elements.<sup>16,20,21</sup> Previous studies of electrolytic cells with buffer-based electrolytes and commercial anion- and cation exchange membranes (A/CEM) have suggested that a > 300 mV pH gradient develops across conventional A/CEM separators under DC polarization, which is only partially mitigated by back diffusion if electroneutral buffers are used.<sup>20</sup>

Bipolar membranes (BPM) have been proposed as an alternative to the conventional A/CEM separators and have been shown to circumvent many system-level challenges associated with coupling earth-abundant catalyst materials and membrane separators in electrolytic cells.<sup>25–36</sup> BPMs composed of two oppositely charged ion exchange layers are beneficial in several respects. First, incorporating a BPM into the cell allows for the separation of acidic and basic solutions in the cathode and anode compartments, respectively, thus providing optimal pH conditions for HER and oxygen evolution reaction (OER) catalysts.<sup>2,3</sup> Second, under reverse bias, *i.e.*, with the cation exchange layer (CEL) facing the cathode, the water dissociation reaction that occurs in the membrane replenishes the cathode and anode with H<sup>+</sup> and OH<sup>−</sup>, respectively, minimizing electrolyte adjustments.<sup>25,32</sup> Finally, the pH gradient at the BPM/electrolyte interface is mitigated due to the predominance of H<sup>+</sup>/OH<sup>−</sup> species inside the CEL/AEL, which match the principal charge carriers in the electrolyte. As a result, most of the cross-membrane potential drop occurs at the CEL/AEL interface, justifying the focus on tailoring the interfacial structure of the BPM in much of the current research on this problem.<sup>37–40</sup> A BPM with a 3D interfacial junction has recently been shown to enable water electrolysis at a current density of 1 A cm<sup>−2</sup> in 0.5 M Na<sub>2</sub>SO<sub>4</sub> solution at membrane potential drop of 2 V.<sup>39</sup> The incorporation of different water dissociation catalysts into the interfacial layer has also been intensively studied.<sup>37,38,40,41</sup> At the interface, water molecules dissociate into H<sup>+</sup> and OH<sup>−</sup> ions, and that reaction is critical to the overall performance of the BPM.

It is widely accepted that the large electric field created under reverse bias and the catalyst in the interfacial region of the BPM dramatically enhance the rate of water dissociation at the AEL/CEL junction, but the relative importance and correlation of these two factors remains unknown. Two effects, namely the second Wien effect, in which an electric field increases the water dissociation rate by orders of magnitude relative to its value in a field-free solution, and a catalytic effect involving proton transfer to a weak base, have been investigated in various models.<sup>42–48</sup> By making an analogy to a p–n junction, an abrupt junction model considers the electric field according to absolute rate theory with the field increasing the generation rate in the forward direction.<sup>42,46</sup>

Based on Onsanger's weak electrolyte theorem and assuming that water can be viewed as a weak electrolyte, the forward dissociation rate constant is simplified to be an electric field-dependent variable.<sup>49</sup> Even though the abrupt junction model correctly predicts the DC polarization behavior of the BPM and the existence of one semicircle in the complex plane of impedance spectra at high reverse bias current,<sup>42,43,50–53</sup> it has been speculated that an unrealistically high electric field would be required if the field-enhanced effect were the sole mechanism for water autodissociation.<sup>46</sup> The treatment of catalyst's role follows the reasoning of Simons, where the catalyst participates in the water dissociation reaction *via* a protonation–deprotonation mechanism.<sup>43,44,46,47</sup>

In principle, a model that couples ionic transport, electrostatics and the field-dependent water dissociation reaction should represent the BPM system realistically and shed light on the correlation between the electric field and the catalyst in accelerating the water dissociation reaction. Unfortunately, unlike its monopolar ion exchange membrane counterpart, an analytical solution to equations of such complexity in the BPM system is not available at this time. Attempts at numerical simulations of the BPM have shown only certain aspects of BPM behaviour because of the lack of one or more of the factors mentioned above.<sup>45</sup> More importantly, an experimental investigation of the roles of the electric field and junction catalyst has been challenging due to the coexisting nature of the two and the sensitivity of the water dissociation reaction to the structure of the interfacial layer.

In the present study, we explore the correlation between the electric field and the junction catalyst in promoting the water dissociation reaction in BPMs. To systematically and controllably adjust the interfacial structure, we prepared a lightly crosslinked AEL with a flat surface<sup>54–56</sup> and modified it with graphite oxide (GO)<sup>32,37,57</sup> as the catalyst using layer-by-layer (LBL) assembly,<sup>58</sup> followed by deposition of a Nafion thin film from a solution in dimethylformamide (DMF) as the CEL. BPMs with one layer and four layers of GO as the junction catalyst were tested by using electrochemical impedance spectroscopy (EIS) and compared against a BPM without a GO catalyst. Interestingly, we observed a counterbalanced role of the electric field and the catalyst in promoting water dissociation. Incorporating the catalyst decreases the electric field intensity across the BPM junction. A numerical simulation model taking into account the ionic transport, electrostatics and electric field-dependent dissociation reaction confirmed our experimental findings. Furthermore, EIS measurements on a BPM with a 3D junction substantiate the conclusions from the numerical model. Finally, the as-prepared BPM shows a significantly lower cross-membrane potential drop than a commercial BPM at > 100 mA cm<sup>−2</sup> current density and has comparable stability over a 10 hour test.

## Results and discussion

### BPM fabrication from a crosslinked anion exchange membrane by layer-by-layer assembly of graphite oxide

BPMs were prepared from a lightly crosslinked AEM and Nafion dissolved in DMF and deposited at 120 °C as the CEL. The

relatively high processing temperature and the DMF solvent alleviate the rod-like aggregation that occurs in lower temperature alcohol/water Nafion dispersions.<sup>59,60</sup> GO layers were deposited as the junction catalyst with poly-diallyldimethylammonium (PDDA) as the polycation using LBL assembly to allow for precise control over the interfacial structure (Fig. 1). From cross-sectional SEM images of the BPM, an AEL of about 100  $\mu\text{m}$  and CEL of about 40  $\mu\text{m}$  thickness can be clearly distinguished, whereas the GO interfacial layer is too thin to be imaged by this technique.

### Balance between the electric field and catalyst in enhancing water dissociation

BPMs with one and four layers of GO were prepared by LBL assembly. EIS measurements were performed while systematically varying the reverse bias on the 1GO and 4GO BPMs and compared with results from a BPM fabricated without catalyst as a control, 0GO BPM. EIS measurements were carried out in a four-electrode cell (see Fig. S1, ESI<sup>†</sup>) in which current was applied through outer Pt working and counter electrodes and the potential was measured between Ag/AgCl (3 M NaCl) reference electrodes (RE) positioned close to the faces of the BPM *via* Haber-Luggin capillaries. This arrangement minimized the effects of solution resistance and eliminated the overpotentials for the HER and OER, as well as

the electrode double-layer capacitance at the Pt working (WE) and counter electrodes (CE) in the EIS measurements and the  $J$ - $E$  curves. An extra CEM was also incorporated between the WE and one of the REs to prevent interference from electrolysis products (Fig. S1, ESI<sup>†</sup>). An AEM was placed between the CE and the other REs for the same reason.

A DC current was initially applied *via* the working and counter electrodes to reach steady-state conditions, and EIS data were then acquired by applying a small amplitude AC signal. The typical Nyquist plots exhibit two semicircles in which the lower frequency semicircle contracts with increasing reverse bias (Fig. S2–S4, ESI<sup>†</sup>). An equivalent circuit developed from the neutral layer model was used to fit all the experimental spectra as we believe that (1) the incorporation of the GO catalyst layer into the BPM can be better described by a model that treats the BPM interfacial layer explicitly and (2) an abrupt junction is unlikely to exist in BPMs prepared by the method shown in Fig. 1.<sup>42,44,53</sup> The overall impedance was then modeled by the series connection of a Gerischer element, an Ohmic resistor representing the membrane and bulk electrolyte, and a block consisting of a resistor and a capacitor (Fig. S2, ESI<sup>†</sup>). A detailed discussion of what each element represents physically is found in the ESI.<sup>†</sup> The quality of the EIS fitting to the equivalent circuit was confirmed by noting the parameter  $\chi^2$ , showing a value of  $\sim 0.01$  and  $\sim 0.003$  for the 4GO and 0GO BPM (Fig. S3 and S4, ESI<sup>†</sup>), respectively.

Fig. 2a compares  $J$ - $E$  curves of the BPMs under reverse bias ranging from 0.6 V to 1.5 V. All BPMs had similar co-ion leakage current density, which is below  $0.5 \text{ mA cm}^{-2}$ , as indicated by the flat portion of the  $J$ - $E$  curve between 0.6 and 0.7 V. Above 0.75 V the current increases significantly as the dominant current-carrying ions in the CEL and AEL become  $\text{H}^+$  and  $\text{OH}^-$ , respectively. The dissociation of water, reaction (1), has a formal



potential (at unit activity of  $\text{H}^+$  and  $\text{OH}^-$ ) of 0.83 V at room temperature,<sup>37</sup> close to observed onset bias. Beyond the onset potential, the 4GO BPM has the lowest overpotential at a given current density, followed by the 1GO BPM, which has much higher current density than the 0GO BPM within the studied reverse bias range.

The water dissociation rate constants,  $k_d$ , of all BPMs increase with increasing bias (Fig. 2b). This suggests that water dissociation is enhanced by the electric field, irrespective of the presence of a catalyst. To be specific, the 0GO and 1GO BPMs show appreciable increases in  $k_d$  at voltages between 0.8 to 0.9 V (Fig. 2b). In contrast,  $k_d$  for the 4GO BPM is relatively large at low reverse bias and increases with increasing voltage. Our attempts to extract accurate values of  $k_d$  at reverse bias potentials  $> 1.1$  V were not successful because the lower frequency semicircles in the EIS spectra become very small and noisy (Fig. S3 and S4, ESI<sup>†</sup>).

Fig. 2c shows the reaction resistance,  $R_w$ , as extracted from the electric double layer (EDL) in the EIS equivalent circuit (Fig. S2, ESI<sup>†</sup>). The BPMs fabricated from the AEL plus Nafion

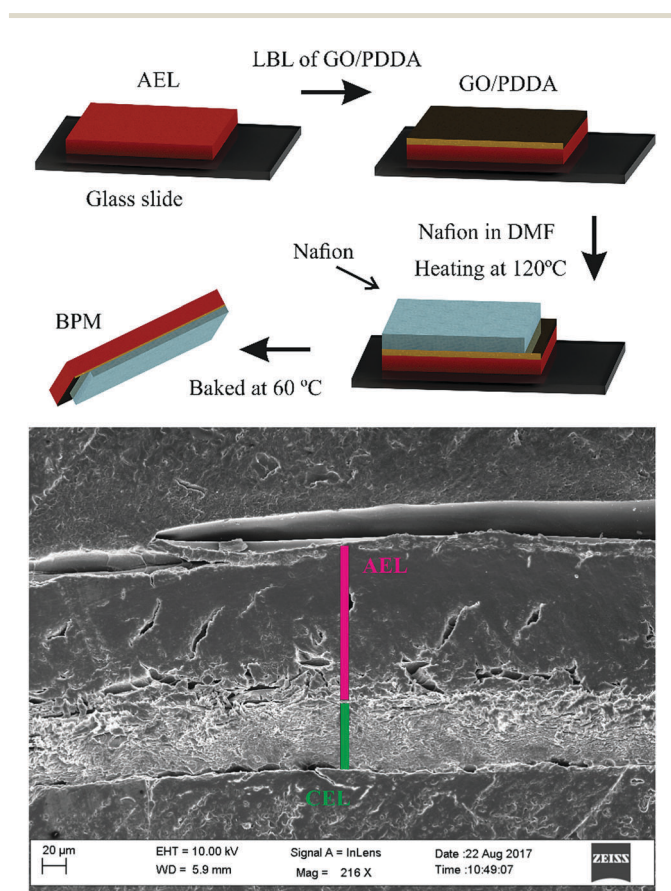


Fig. 1 Schematic of the preparation of BPMs by LBL assembly, and a cross-sectional scanning electron micrograph (SEM) image of the 4GO BPM. The green and red lines span the CEL and AEL, respectively.

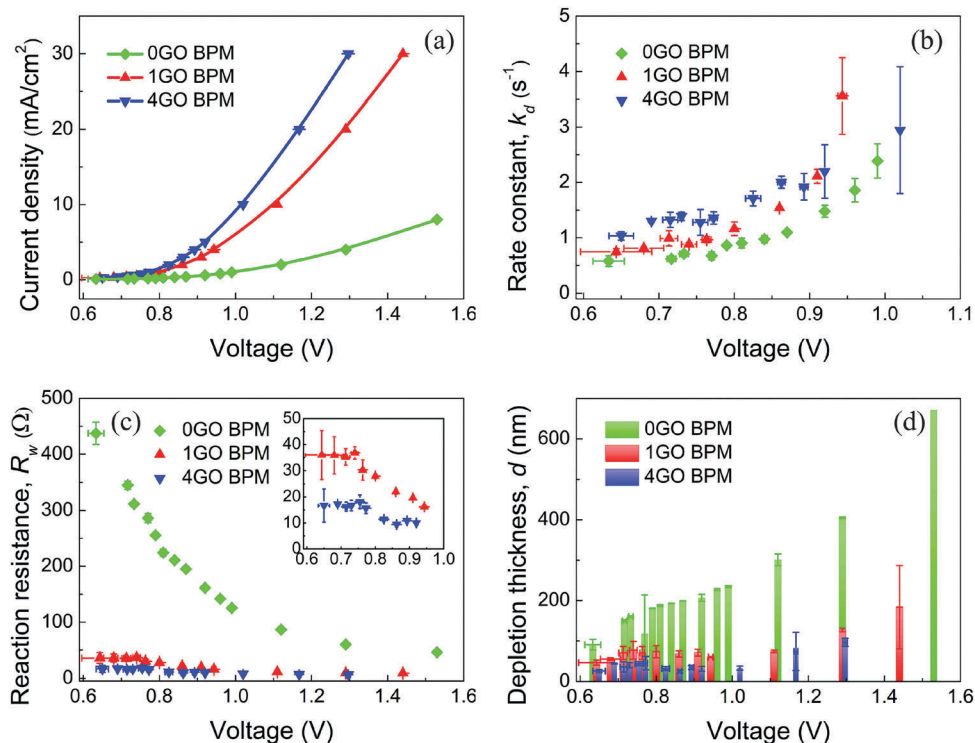


Fig. 2 (a)  $J$ - $E$  curves of BPMs prepared by the LBL technique, in 0.5 M  $\text{KNO}_3$  at low reverse bias, which is also the bias range used in the EIS study. 0GO/1GO/4GO BPM correspond to BPMs with zero/one/four layers of GO catalyst; (b) water dissociation rate constant  $k_d$  measured from the Gerischer element; (c) water dissociation reaction resistance  $R_w$ ; inset shows an enlarged view at lower voltage; (d) depletion region thickness as a function of reverse bias voltage. Error bars in (a) and (c) are shown for cases where they are larger than the plot symbols.

share the same trend in  $R_w$ , *i.e.*, that it decreases as voltage increases and gradually converges to a plateau (Fig. 2c). The flat portion of the curve corresponds to a quasi-equilibrium region for the water dissociation reaction, where the forward dissociation and backward neutralization reaction rates cancel each other and are equal to the exchange current.<sup>44</sup> Before reaching the quasi-equilibrium region, the dissociation reaction is largely suppressed because of the fast backward acid-base neutralization reaction. An increase in reverse bias helps promote the dissociation reaction, thus decreasing  $R_w$ . The 4GO BPM exhibited the lowest  $R_w$  within the studied voltage range, compared to the 0GO and 1GO BPMs, indicating that the forward dissociation reaction is promoted more efficiently with more added catalyst (Fig. 2c). The dependence of  $R_w$  on voltage is much weaker for the 1GO/4GO BPMs, suggesting a lower electric field in BPMs that contain catalyst layers. It is noteworthy that the different reaction resistances,  $R_w$ , between these synthetic BPMs cannot be simply attributed to the co-ion leakage effect, since all BPMs had similar leakage current density (Fig. 2a), but very different values of  $R_w$ .

In the neutral layer model, a reaction layer in which the water dissociation reaction becomes prevalent and produces nearly the total amount of  $\text{H}^+$  and  $\text{OH}^-$  required for a given current density is sandwiched by an EDL formed from the unbalanced fixed charge density on the CEL and AEL sides.<sup>43,44</sup> This unbalanced charge is a consequence of the depletion of ions under reverse bias conditions, resulting in the formation

of a depletion region. The depletion layer thickness can be calculated from eqn (2):

$$d = \frac{\varepsilon_0 \varepsilon_r A}{C} \quad (2)$$

where  $\varepsilon_0$  and  $\varepsilon_r$  are respectively the vacuum electric permittivity and the dielectric constant in the reaction layer (80 was taken for pure water), and  $C$  and  $A$  are the capacitance and active membrane area (1 cm<sup>2</sup>). The capacitance  $C$  was calculated based on eqn (S7) and (S8) (ESI<sup>†</sup>). The values of the capacitance and the depletion layer thickness as a function of reverse current are recorded in Tables S1, S2 and S3 for 4GO, 1GO and 0GO BPM, respectively (ESI<sup>†</sup>), along with other parameters from the EIS fitting. The validity of calculating the depletion layer thickness from EIS fitting scheme is further confirmed by repeating the modeling process of the EIS spectra for the 0GO BPM with a fixed (average) depletion thickness (other parameters were allowed to float freely). The resulting  $\chi^2$  value of 0.03–0.6 was much larger than those from the fitting where depletion layer thickness was optimized, 0.001–0.003 (red vs. green lines, Fig. S4, ESI<sup>†</sup>).

With the method outlined above, we obtained a depletion layer thickness,  $d$ , on the scale of hundreds of nanometers for the 0GO BPM and tens of nanometers for the 1GO and 4GO BPMs (Fig. 2d). As shown in Fig. 2d, the depletion thickness  $d$  is much smaller for the 1GO and 4GO BPMs than it is for the 0GO BPM. The key findings from this analysis are the thinner

depletion region and weaker dependence on electric potential with increasing catalyst loading. This indicates that there is a smaller electric field acting on the reaction layer in BPMs that contain water dissociation catalysts, which will be evident from the results of the numerical modeling below.

### Insights from a numerical simulation model

To gain further insight into the experimental data, we constructed a numerical model that takes into account ionic transport, electrostatics, and the rates of the water dissociation/recombination reactions.<sup>45,61,62</sup> In order to fully address the characteristics of BPMs, it is necessary to identify the mechanisms that participate in the ionic transport of both the electrolyte and water dissociation products under bias as well as the water dissociation/recombination reaction. A large body of previous work devoted to the theoretical understanding of various phenomena in ion exchange membranes is based on the Nernst–Planck–Poisson equations (NPP), where the Nernst–Planck equation (eqn (S9), ESI†) describes ionic transport and maintains species continuity and the Poisson equation describes the fixed charge and the ion permselectivity (eqn (S10), ESI†).<sup>63–65</sup> Incorporating the water dissociation reaction is achieved by adding a flux term in the transport equation for  $H^+$  and  $OH^-$ , which also affects the whole system electrostatically by modifying the bulk charge density. The reaction rate can be obtained from a kinetic model for the dissociation and recombination of  $H^+$  and  $OH^-$ , with a forward rate constant that depends on the electric field

and a field-independent recombination rate constant (eqn (S11) and (S12), ESI†).<sup>44,47</sup> Two diffusion boundary layers were added at the two faces of the BPM in order to better match the experimental conditions, and this turns out to be important in modeling the BPM under higher reverse bias.

The analysis of the model begins with predictions of the  $J$ – $E$  curve and potential distribution profile at equilibrium. Fig. 3a shows the current density at a given reverse bias and its comparison with experiment. The agreement of the overall current density between experiment and simulation is satisfactory at low reverse bias, whereas the deviation increases under higher bias. This deviation could be caused by the static boundary conditions employed in the model, which result in unrealistic concentration profiles, as will be discussed below. The overall current density is decomposed into the contributions from water dissociation products  $H^+/OH^-$  and from supporting electrolyte  $K^+/NO_3^-$ . As expected, the  $H^+/OH^-$  flux surpasses that of  $K^+/NO_3^-$  only after a certain reverse bias threshold, 2 V (Fig. 3a), after which the water dissociation reaction is enhanced dramatically by the electric field according to the second Wien effect.<sup>42,49</sup> It has been shown that hysteresis develops in the  $J$ – $E$  curve of BPMs that are subjected to a time-periodic reverse voltage due to the incomplete depletion of mobile ions at the junction, and the magnitude of the hysteresis depends on the scan rate.<sup>61</sup> The absence of hysteresis in the  $J$ – $E$  curve (Fig. 3a), is consistent with these observations as the current model simulates the steady-state response. Under a reverse bias less

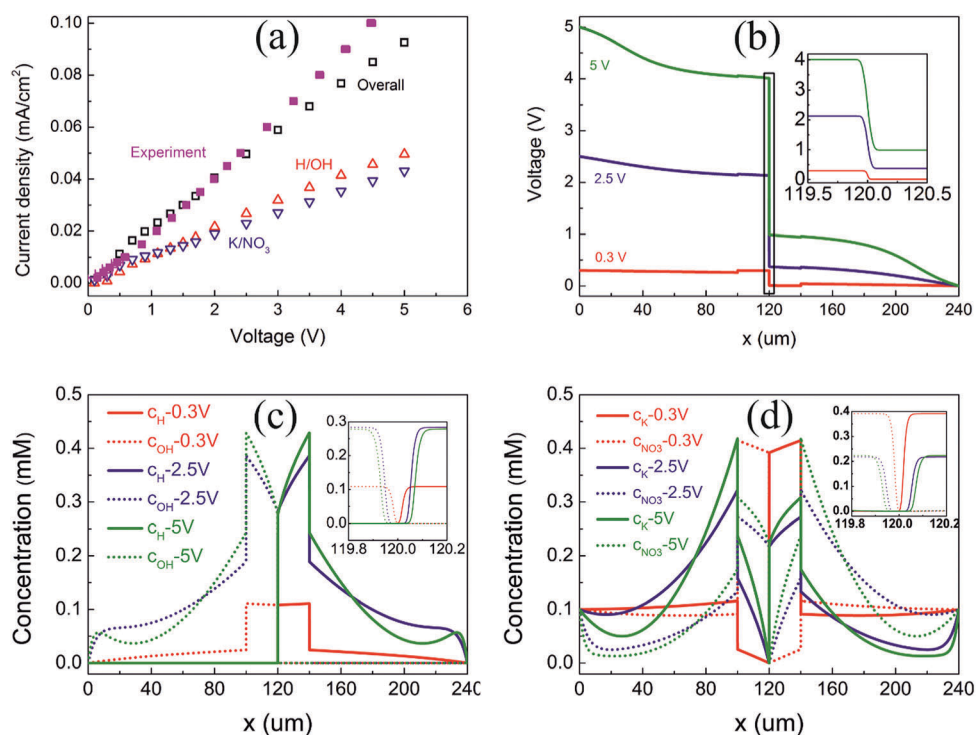


**Fig. 3** Numerical simulations of a BPM with catalyst. (a) Simulated  $J$ – $E$  curve of a BPM with catalyst, and comparison with experimental results. The experimental  $J$ – $V$  curve shown was obtained for 1GO BPM in 0.1 mM  $KNO_3$  in order to match the conditions of the simulation; also shown are the current contributions from water dissociation products and from the electrolyte,  $KNO_3$ ; (b) potential distributions from the simulation; (c) concentration profiles of the water dissociation products  $H^+$  and  $OH^-$  in the BPM; (d) electrolyte  $KNO_3$  ion distributions. Insets in (b)–(d) are enlarged version of the AEL/CEL junction region. The fixed charged density of the AEL/CEL in the simulation was set to 0.5 mM to speed up the convergence.

than 5 V, more than 90% of the potential drop occurs across the BPM junction (Fig. 3b). At larger reverse bias of 5 V, there is an appreciable potential drop in the region of electrolyte close to the boundary (Fig. 3b). We attribute this potential drop to the low  $\text{H}^+/\text{OH}^-$  concentration at the two boundaries, which limits the achievable  $\text{H}^+/\text{OH}^-$  flux under higher reverse bias (Fig. 3c). This also gives rise to an underestimate of the  $\text{H}^+/\text{OH}^-$  contribution to the overall current density as shown in Fig. 3a. Improvement of the model may be possible by using dynamic boundary conditions.

Fig. 3c and d show the concentration profiles of  $\text{H}^+/\text{OH}^-$  and  $\text{K}^+/\text{NO}_3^-$  at reverse biases of 0.3 V, 2.5 V and 5 V. These concentration profiles were found to be representative of the overall concentration distributions as the reverse bias varies (Fig. S6, ESI<sup>†</sup>). At lower reverse bias, the supporting  $\text{K}^+/\text{NO}_3^-$  ions are the major charge carriers inside both the BPM and diffusion layers. In contrast, water dissociation products  $\text{H}^+$  and  $\text{OH}^-$  become the dominant ionic species under higher reverse bias, expelling  $\text{K}^+$  and  $\text{NO}_3^-$  from the bulk of the membrane and accumulating in the diffusion boundary layers. The insets in Fig. 3c and d illustrate the formation of a depletion region at the AEL/CEL interface, the thickness of which increases with increasing reverse bias.

In order to assess the effectiveness of the catalyst, results from the model without the catalytic effect (Fig. S7, ESI<sup>†</sup>), were compared with the BPM with catalyst, which enhances the dissociation rate constant by two orders of magnitude (Fig. 3). Lower current density is observed at a given reverse bias compared with the BPM with catalyst (Fig. S7a, ESI<sup>†</sup>). As expected, the  $\text{H}^+/\text{OH}^-$  flux is also smaller than that of the BPM with catalyst due to the lower reaction rate constant. The onset reverse bias at which the  $\text{H}^+/\text{OH}^-$  flux start to dominate

over that of  $\text{K}^+/\text{NO}_3^-$  is lower for the BPM with catalyst, *i.e.* 2 V vs. 4.5 V. The potential and concentration distribution profiles for BPMs with and without catalyst resemble each other. Furthermore, to check the consistency of the model, results for the BPM without catalyst were subjected to forward bias conditions, as shown in Fig. S8 (ESI<sup>†</sup>). Current contributed from  $\text{H}^+/\text{OH}^-$  flux is marginally small for the studied voltage range, and the BPM shows typical Ohmic resistance (Fig. S8a, ESI<sup>†</sup>). The predominant charge carriers in the BPM and diffusion boundary layers are those from the supporting electrolyte at all voltages (Fig. S8c and d, ESI<sup>†</sup>). One striking difference from BPMs under reverse bias is the absence of the depletion region, which is replaced by a smooth transition of one type of charge carrier to another. These results are in good agreement with recent theoretical reports on BPMs in fuel cell applications where forward bias and the backward recombination reaction are more relevant.<sup>62,66,67</sup> Interestingly, most of the potential drop under forward bias conditions happens across the diffusion layer (Fig. S8b, ESI<sup>†</sup>), rather than at the AEL/CEL junction, due to the high concentration of ions present.

Having established the validity of the numerical model, we extracted the electric field intensity at the AEL/CEL interface and calculated the depletion region thickness based on the method outlined in Fig. S9 (ESI<sup>†</sup>). Fig. 4 compares the electric field intensity and depletion layer thickness for BPMs with and without catalyst. Consistent with the experimental observations (Fig. 2d), a thinner depletion region is found for the BPM with catalyst (Fig. 4d), leading to a smaller electric field across the AEL/CEL interface (Fig. 4c). The difference can be understood as a result of the counterbalanced roles of electric field and catalyst in promoting water dissociation (Fig. 4a and b).

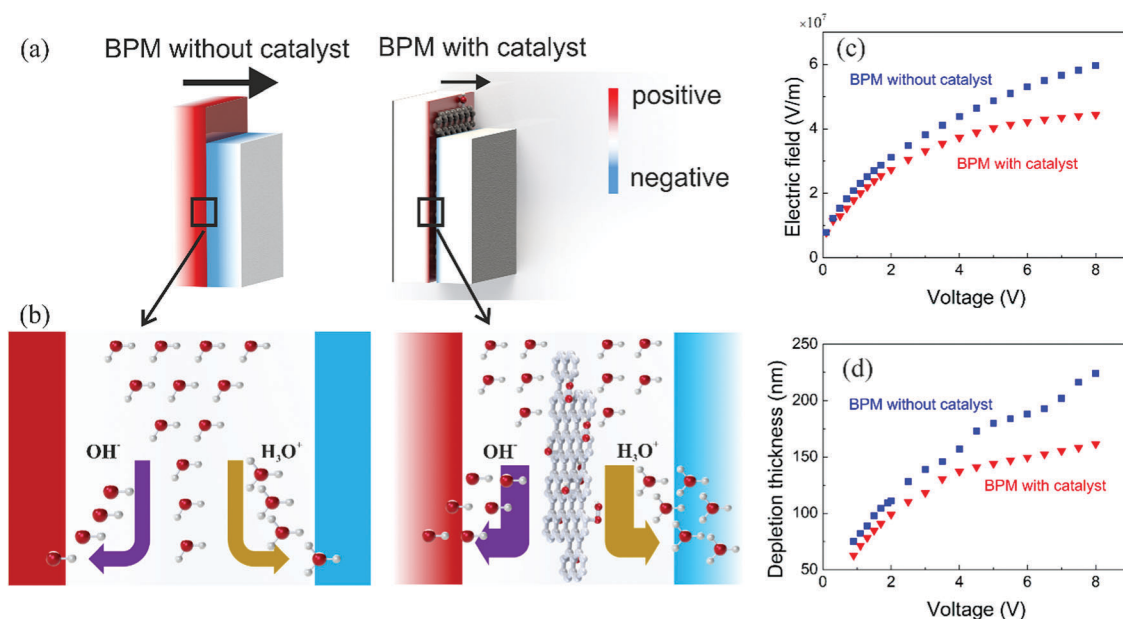


Fig. 4 Schematic drawings of (a) the depletion region for BPMs with and without catalyst and (b) an enlarged view of the junction region, showing the higher  $\text{H}^+/\text{OH}^-$  flux in the BPM with catalyst. The black arrows indicate the higher electric field in the BPM without catalyst; the red/blue colors indicate the positive/negative fixed charges in AEL/CEL, respectively. Simulated (c) electric field intensity at the AEL/CEL interface and (d) depletion region thickness for BPMs with and without catalyst.

Under reverse bias, mobile ions in the BPM are driven out so that a depletion region forms due to the unbalanced fixed charge on the CEL and AEL layers. The resulting electric field enhances water dissociation and produces overwhelmingly a flux of  $\text{H}^+$  and  $\text{OH}^-$  ions towards the CEL and AEL of the BPM, respectively. As such, the unbalanced fixed charge density is partially neutralized by the respective counter ions, *i.e.*  $\text{H}^+$  for the CEL and  $\text{OH}^-$  for the AEL, hence shrinking the depletion region. Since the  $\text{H}^+/\text{OH}^-$  flux for the BPM with catalyst is much larger than that without catalyst (Fig. S7a, ESI<sup>†</sup>), a larger portion of the fixed charge is rebalanced (Fig. 4b), causing the electric field across the reaction layer to decrease.

### High $\text{H}^+/\text{OH}^-$ flux achieved through a 3D junction

Pintauro *et al.* recently reported a novel type of BPM with a diffuse 3D junction by combining single and dual polymer fiber electrospinning.<sup>39</sup> The BPM has been shown to sustain at  $1 \text{ A cm}^{-2}$  reverse-bias current density with less than 2 V of transmembrane potential drop in 0.5 M  $\text{Na}_2\text{SO}_4$ . The low membrane impedance has been attributed to the 3D extended junction region for the water dissociation reaction. Fig. 5 shows an SEM image of the 3D junction region with intertwined AEL and CEL fibers (Fig. 5a), a schematic of the 3D BPM (Fig. 5b, left), and an enlarged schematic of the junction region (Fig. 5b, middle and right). The intimate contact between the

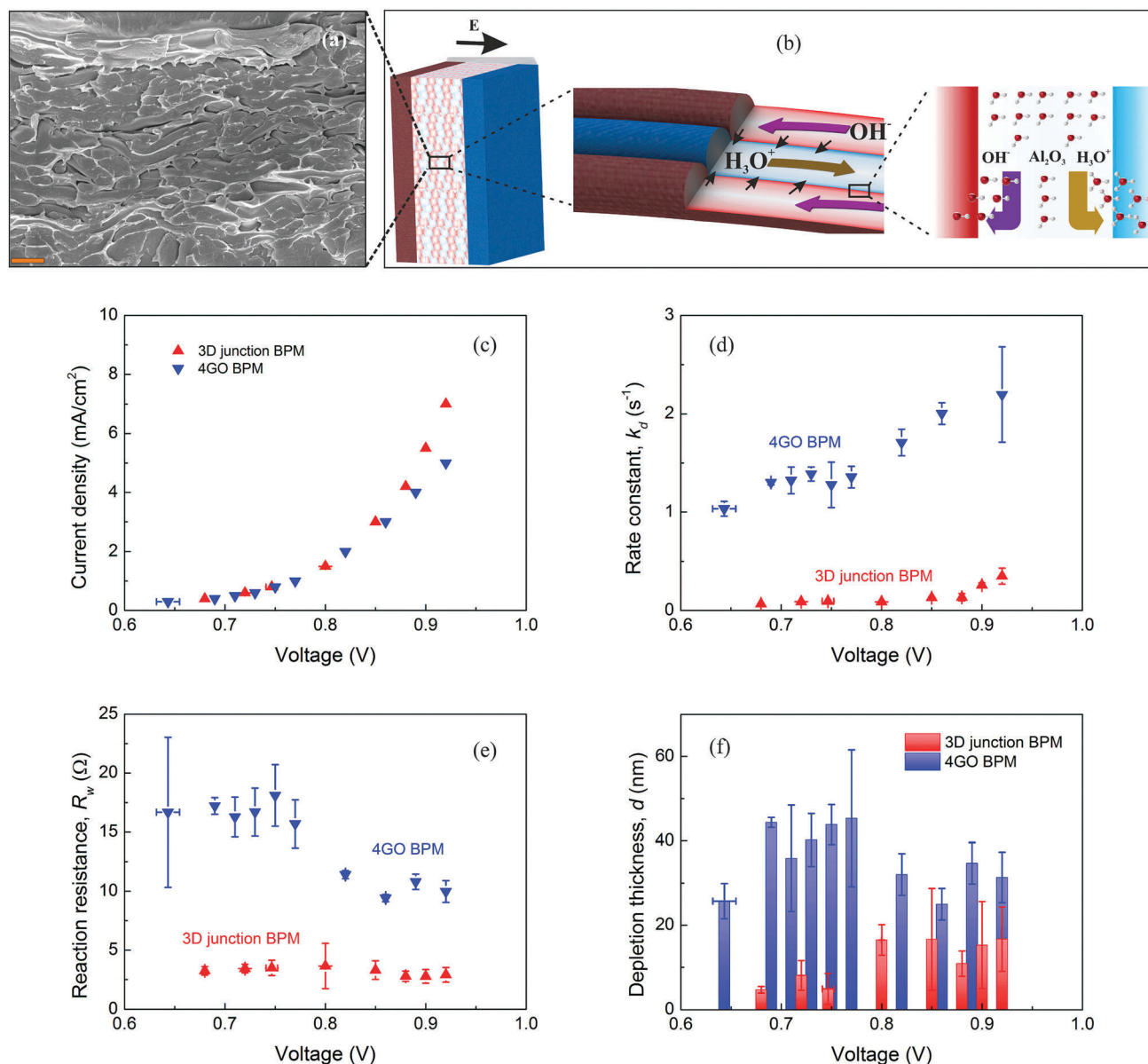


Fig. 5 BPM with a 3D junction. (a) SEM image of the junction region, the scale bar corresponds to  $20 \mu\text{m}$ ; (b) (left): schematic of the 3D junction BPM, with AEL (red), CEL (blue) and dual-fiber junctions. (middle): Enlarged view of the dual fiber junction. The mixture of AEL and CEL fibers in the junction region provide pathways for  $\text{H}^+$  and  $\text{OH}^-$  transport. Black arrows in the left and middle panels indicate the overall and local electric fields, respectively. (right): Enlarged view of the AEL/CEL interface in the junction region, where water dissociates into  $\text{H}^+$  and  $\text{OH}^-$  at the  $\text{Al}_2\text{O}_3$  catalyst; (c)  $J$ - $E$  curves of 3D junction and 4GO BPM in 0.5 M  $\text{KNO}_3$  at lower reverse bias; (d) water dissociation rate constant  $k_d$ ; (e) water dissociation reaction resistance  $R_w$ ; (f) depletion region thickness  $d$  as a function of reverse bias voltage.

AEL/CEL fibers enabled by DMF vapor treatment and hot pressing in the junction provides multiple transport pathways for water dissociation products  $\text{H}^+$  and  $\text{OH}^-$  and greatly facilitates their removal from the junction region (Fig. 5b, middle). Consequently, a large  $\text{H}^+/\text{OH}^-$  flux and faster water dissociation are expected in the 3D junction of the BPM, which was experimentally confirmed below. As shown above, a large ion flux from water dissociation should compensate for the unbalanced fixed charge in the AEL and CEL and decrease the electric field across the junction region. In addition, unlike in the planar junction BPM, in which the electric field is applied perpendicular to the depletion layer plane, the 3D junctions span a range of angles to the membrane plane, as evidenced in the SEM image of the junction (Fig. 5a). This effect lowers the local electric field across the dispersed AEL/CEL fiber interface and thus further reduces the overall electric field (Fig. 5b, left and middle).

Developing an accurate model for the 3D BPM is challenging due to the interpenetrating structure within the junction region. However, the same neutral layer model was taken to interpret the EIS data in the 3D BPM. On the one hand, the basic working principle of the 3D junction BPM is the same as that of the 2D BPM (Fig. 5b). It is the intimate local contact between the AEL and CEL that distinguishes the 3D interface from its 2D counterpart. However, the neutral layer model does not take into account the microstructure of the reaction region.<sup>44</sup> On the other hand, the EIS spectra collected for 3D junction BPM do resemble its 2D counterpart, Fig. S5 (ESI<sup>†</sup>), except for the detailed shape at higher frequency region.

Under steady-state galvanostatic polarization, the 3D junction BPM exhibits a similar co-ion leakage current as the 4GO BPM at lower reverse bias in a pH neutral electrolyte (Fig. 5c). The 3D junction BPM shows a nearly constant  $k_d$  up to a reverse bias of  $\sim 0.9$  V (Fig. 5d). It is noteworthy that the observed lower overpotential of the 3D junction BPM does not stem from catalysis of the water dissociation reaction because the 4GO BPM exhibits a relatively larger rate constant  $k_d$ . In stark contrast to the 4GO BPM, the reaction resistance,  $R_w$ , for the 3D junction BPM does not show obvious convergence to a plateau but rather remains almost constant, and is much smaller within the studied voltage

range (Fig. 5e). The lower reaction resistance for the 3D junction BPM is attributed to facilitated water dissociation made possible by the rapid removal of  $\text{H}^+/\text{OH}^-$  through the interpenetrating AEL/CEL fibers, which results in a larger  $\text{H}^+/\text{OH}^-$  flux in the junction region relative to flat interface BPMs. The independence of  $R_w$  on the transmembrane voltage indicates a small electric field in the 3D junction BPM as a result of the large  $\text{H}^+/\text{OH}^-$  flux. The smaller electric field is also verified by the thinner depletion thickness  $d$  compared with that of the 4GO BPM (Fig. 5f).

Finally, it is tempting to consider carrying out EIS measurements of the BPMs under normal operating conditions as in Fig. 6, *i.e.* with acid and base in the cathode and anode compartments, respectively, in order to correlate the water autodissociation kinetics with cell performance under practically relevant conditions. For the purpose of studying the mechanism of water autodissociation and the effects of electric field and catalysis, the pH neutral electrolyte allows us to monitor the gradual formation of the depletion region and the resulting electric field. This was found to be difficult with asymmetric electrolytes, as shown in Fig. S10 (ESI<sup>†</sup>).

### Performance comparison of BPMs at high reverse bias

Fig. 6a compares BPMs with no GO/four layers of GO (0GO/4GO BPM), and the 3D junction BPM with a commercial Fumatech BPM in terms of the potential drop across the membrane at a given reverse bias current density. At low current density, the cross-membrane potential is similar for all membranes except the 0GO BPM, whereas at current densities greater than  $100 \text{ mA cm}^{-2}$ , the 4GO and 3D junction BPMs show significantly lower potential drop than the Fumatech BPM. The characteristics of the BPM current density–voltage ( $J$ – $E$ ) curve have been thoroughly discussed in the literature.<sup>37,40</sup> Galvanostatic measurements at a reverse-bias current density of  $100 \text{ mA cm}^{-2}$  were performed and the results (Fig. 6b) suggest that both membranes were stable for at least 10 hours of continuous operation. The moderate increase in the cross-membrane potential for the 4GO BPM may be associated with degradation of GO in the interfacial layer during operation.

Compared with the BPM with no catalyst, 0GO BPM, the cross-membrane potential of the 4GO BPM is much lower at all studied reverse bias values (Fig. 6a) due to the smaller water

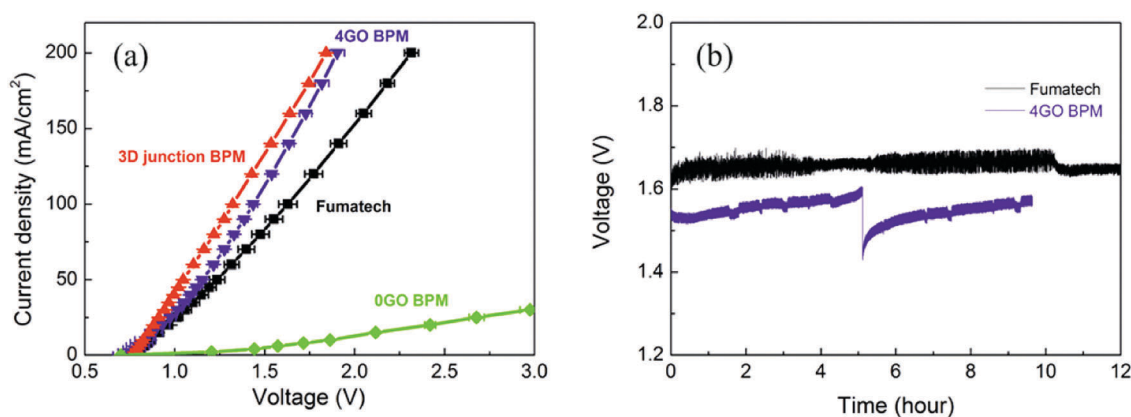


Fig. 6 (a)  $J$ – $E$  curves of BPMs, measured with 0.5 M HCl and 0.5 M KOH in the cathodic and anodic chambers, respectively; (b) steady-state performance of BPMs, measured under reverse bias of  $100 \text{ mA cm}^{-2}$ ; the dip in 4GO BPM is due to the removal of bubbles.

dissociation reaction resistance,  $R_w$ , of the latter (Fig. 2c). The depletion layer thickness and thus the electric field in the 0GO BPM are larger than those of the BPM with catalyst, 4GO BPM, and show a clear dependence of increasing as the reverse bias increases (Fig. 2d). For the 0GO BPM, a wider depletion region gives rise to a stronger electric field, which promotes water dissociation to a larger extent so that the produced  $H^+/OH^-$  flux matches the higher current density at an increased reverse bias. However, for the 4GO BPM, the catalyst provides an alternative means of enhancing the rate of water dissociation. As such, the depletion region and electric field do not need to be as enlarged in order to achieve the same current density.

Similarly, the electric field in the 3D junction BPM is also shown to be small (Fig. 5f). Two origins for the small electric field in the 3D junction BPM are: (1) the large  $H^+/OH^-$  flux due to the facile transport of the charged species because of the interpenetrating AEL/CEL dual fiber structure, compared to the incorporation of an effective catalyst as considered in the 4GO BPM and (2) the wide range of angles spanned by the AEL/CEL interfaces with respect to the overall electric field. Because of this effect, improving the membrane fabrication process so that the AEL/CEL interfaces are more perpendicular to the membrane plane would be expected to impart a larger role to the electric field in 3D junction BPMs.

## Conclusion

In summary, BPMs were prepared from a crosslinked AEL and Nafion CEL with a GO catalyst deposited in between by LBL assembly, allowing for precise control of the interfacial structure. By adjusting the GO catalyst layers, a balance between the second Wien effect and the catalytic effect in promoting water dissociation has been discovered. A comprehensive numerical simulation model elucidated that the electric field enhancement for water dissociation may be compromised by incorporating catalysts into the BPM junction, as that produces a larger  $H^+/OH^-$  flux that partially mitigates the net fixed charge on AEL and CEL of the BPMs. This conclusion is further corroborated by testing a 3D junction BPM, which exhibits a large  $H^+/OH^-$  flux because of facilitated ionic transport through the interpenetrating junction. This quantification of the balancing role of electric field and catalyst in promoting water dissociation implies a crucial rule of the catalyst layer under higher reverse bias conditions and should help guide the design of higher performance BPMs. In particular, the diminished role of the second Wien effect at higher reverse bias for BPMs with catalyst layers implies that for applications in which high current density is desirable, increasing the effectiveness of the catalysis is the best solution. For the 3D BPM, modifying the fabrication procedure to orient the AEL/CEL interface perpendicular to the membrane plane would enable the electric field to play a larger role in accelerating water dissociation.

## Conflicts of interest

There are no conflicts to declare.

## Disclaimer

This report was prepared as an account of work sponsored by an agency of the United States Government. Neither the United States Government nor any agency thereof, nor any of their employees, makes any warranty, express or implied, or assumes any legal liability or responsibility for the accuracy, completeness, or usefulness of any information, apparatus, product, or process disclosed, or represents that its use would not infringe privately owned right. Reference herein to any specific commercial product, process, or service by trade name, trademark, manufacturer, or otherwise does not necessarily constitute or imply its endorsement, recommendation, or favoring by the United States Government or any agency thereof. The views and opinions of authors expressed herein do not necessarily state or reflect those of the United States Government or any agency thereof.

## Acknowledgements

Z. Y. would like to thank Mr Chuanyu Yan (Luxembourg Institute of Science and Technology) for assisting in the setup of the four-chamber measurement and Mr Pengtao Xu for help in formatting of the paper. This work was supported by the Office of Basic Energy Sciences, Division of Chemical Sciences, Geosciences, and Energy Bioscience, Department of Energy under contract (DE-FG02-07ER15911), and by the Canadian Institute for Advanced Research. Anion exchange membrane synthesis was supported by the DOE-NETL University Coalition for Fossil Energy Research (UCFER) under DOE Award Number DE-FE0026825. M. A. H. acknowledges the Corning Foundation and the Corning Faculty Fellowship in Materials Science and Engineering for support.

## References

- 1 N. S. Lewis, Research opportunities to advance solar energy utilization, *Science*, 2016, **351**, aad1920.
- 2 C. C. L. McCrory, S. Jung, J. C. Peters and T. F. Jaramillo, Benchmarking Heterogeneous Electrocatalysts for the Oxygen Evolution Reaction, *J. Am. Chem. Soc.*, 2013, **135**, 16977–16987.
- 3 C. C. L. McCrory, S. Jung, I. M. Ferrer, S. M. Chatman, J. C. Peters and T. F. Jaramillo, Benchmarking Hydrogen Evolving Reaction and Oxygen Evolving Reaction Electrocatalysts for Solar Water Splitting Devices, *J. Am. Chem. Soc.*, 2015, **137**, 4347–4357.
- 4 A. L. Strickler, M. Escudero-Escribano and T. F. Jaramillo, Core-Shell Au@Metal-Oxide Nanoparticle Electrocatalysts for Enhanced Oxygen Evolution, *Nano Lett.*, 2017, **17**, 6040–6046.
- 5 M. Schreier, F. Héroguel, L. Steier, S. Ahmad, J. S. Luterbacher, M. T. Mayer, J. Luo and M. Grätzel, Solar conversion of  $CO_2$  to CO using Earth-abundant electrocatalysts prepared by atomic layer modification of CuO, *Nat. Energy*, 2017, **2**, 17087.
- 6 C. Kim, H. S. Jeon, T. Eom, M. S. Jee, H. Kim, C. M. Friend, B. K. Min and Y. J. Hwang, Achieving Selective and Efficient Electrocatalytic Activity for  $CO_2$  Reduction Using Immobilized Silver Nanoparticles, *J. Am. Chem. Soc.*, 2015, **137**, 13844–13850.

- 7 T. Hatsukade, K. P. Kuhl, E. R. Cave, D. N. Abram and T. F. Jaramillo, Insights into the electrocatalytic reduction of CO<sub>2</sub> on metallic silver surfaces, *Phys. Chem. Chem. Phys.*, 2014, **16**, 13814–13819.
- 8 S. Liu, H. Tao, L. Zeng, Q. Liu, Z. Xu, Q. Liu and J.-L. Luo, Shape-Dependent Electrocatalytic Reduction of CO<sub>2</sub> to CO on Triangular Silver Nanoplates, *J. Am. Chem. Soc.*, 2017, **139**, 2160–2163.
- 9 C. W. Li and M. W. Kanan, CO<sub>2</sub> Reduction at Low Overpotential on Cu Electrodes Resulting from the Reduction of Thick Cu<sub>2</sub>O Films, *J. Am. Chem. Soc.*, 2012, **134**, 7231–7234.
- 10 Y. Chen, C. W. Li and M. W. Kanan, Aqueous CO<sub>2</sub> Reduction at Very Low Overpotential on Oxide-Derived Au Nanoparticles, *J. Am. Chem. Soc.*, 2012, **134**, 19969–19972.
- 11 C. Rogers, W. S. Perkins, G. Veber, T. E. Williams, R. R. Cloke and F. R. Fischer, Synergistic Enhancement of Electrocatalytic CO<sub>2</sub> Reduction with Gold Nanoparticles Embedded in Functional Graphene Nanoribbon Composite Electrodes, *J. Am. Chem. Soc.*, 2017, **139**, 4052–4061.
- 12 W. Luc, C. Collins, S. Wang, H. Xin, K. He, Y. Kang and F. Jiao, Ag–Sn Bimetallic Catalyst with a Core–Shell Structure for CO<sub>2</sub> Reduction, *J. Am. Chem. Soc.*, 2017, **139**, 1885–1893.
- 13 L.-A. Stern, L. Feng, F. Song and X. Hu, Ni<sub>2</sub>P as a Janus catalyst for water splitting: the oxygen evolution activity of Ni<sub>2</sub>P nanoparticles, *Energy Environ. Sci.*, 2015, **8**, 2347–2351.
- 14 K. P. Kuhl, E. R. Cave, D. N. Abram and T. F. Jaramillo, New insights into the electrochemical reduction of carbon dioxide on metallic copper surfaces, *Energy Environ. Sci.*, 2012, **5**, 7050–7059.
- 15 A. A. Peterson, F. Abild-Pedersen, F. Studt, J. Rossmeisl and J. K. Nørskov, How copper catalyzes the electroreduction of carbon dioxide into hydrocarbon fuels, *Energy Environ. Sci.*, 2010, **3**, 1311–1315.
- 16 M. A. Modestino, S. M. H. Hashemi and S. Haussener, Mass transport aspects of electrochemical solar-hydrogen generation, *Energy Environ. Sci.*, 2016, **9**, 1533–1551.
- 17 S. Chabi, K. M. Papadantonakis, N. S. Lewis and M. S. Freund, Membranes for artificial photosynthesis, *Energy Environ. Sci.*, 2017, **10**, 1320–1338.
- 18 C. Xiang, A. Z. Weber, S. Ardo, A. Berger, Y. Chen, R. Coridan, K. T. Fountaine, S. Haussener, S. Hu, R. Liu, N. S. Lewis, M. A. Modestino, M. M. Shaner, M. R. Singh, J. C. Stevens, K. Sun and K. Walczak, Modeling, Simulation, and Implementation of Solar-Driven Water-Splitting Devices, *Angew. Chem., Int. Ed.*, 2016, **55**, 12974–12988.
- 19 M. Dunwell, Q. Lu, J. M. Heyes, J. Rosen, J. G. Chen, Y. Yan, F. Jiao and B. Xu, The Central Role of Bicarbonate in the Electrochemical Reduction of Carbon Dioxide on Gold, *J. Am. Chem. Soc.*, 2017, **139**, 3774–3783.
- 20 E. A. Hernández-Pagán, N. M. Vargas-Barbosa, T. Wang, Y. Zhao, E. S. Smotkin and T. E. Mallouk, Resistance and polarization losses in aqueous buffer–membrane electrolytes for water-splitting photoelectrochemical cells, *Energy Environ. Sci.*, 2012, **5**, 7582–7589.
- 21 J. Jin, K. Walczak, M. R. Singh, C. Karp, N. S. Lewis and C. Xiang, An experimental and modeling/simulation-based evaluation of the efficiency and operational performance characteristics of an integrated, membrane-free, neutral pH solar-driven water-splitting system, *Energy Environ. Sci.*, 2014, **7**, 3371–3380.
- 22 A. Berger, R. A. Segalman and J. Newman, Material requirements for membrane separators in a water-splitting photoelectrochemical cell, *Energy Environ. Sci.*, 2014, **7**, 1468–1476.
- 23 S. Haussener, C. Xiang, J. M. Spurgeon, S. Ardo, N. S. Lewis and A. Z. Weber, Modeling, simulation, and design criteria for photoelectrochemical water-splitting systems, *Energy Environ. Sci.*, 2012, **5**, 9922–9935.
- 24 A. Ursua, L. M. Gandia and P. Sanchis, Hydrogen Production From Water Electrolysis: Current Status and Future Trends, *Proc. IEEE*, 2012, **100**, 410–426.
- 25 N. M. Vargas-Barbosa, G. M. Geise, M. A. Hickner and T. E. Mallouk, Assessing the Utility of Bipolar Membranes for use in Photoelectrochemical Water-Splitting Cells, *ChemSusChem*, 2014, **7**, 3017–3020.
- 26 J. Luo, D. A. Vermaas, D. Bi, A. Hagfeldt, W. A. Smith and M. Grätzel, Bipolar Membrane-Assisted Solar Water Splitting in Optimal pH, *Adv. Energy Mater.*, 2016, **6**, 1600100.
- 27 R. S. Reiter, W. White and S. Ardo, Communication—Electrochemical Characterization of Commercial Bipolar Membranes under Electrolyte Conditions Relevant to Solar Fuels Technologies, *J. Electrochem. Soc.*, 2016, **163**, H3132–H3134.
- 28 Y. C. Li, D. Zhou, Z. Yan, R. H. Gonçalves, D. A. Salvatore, C. P. Berlinguette and T. E. Mallouk, Electrolysis of CO<sub>2</sub> to Syngas in Bipolar Membrane-Based Electrochemical Cells, *ACS Energy Lett.*, 2016, **1**, 1149–1153.
- 29 D. A. Vermaas, M. Sassenburg and W. A. Smith, Photo-assisted water splitting with bipolar membrane induced pH gradients for practical solar fuel devices, *J. Mater. Chem. A*, 2015, **3**, 19556–19562.
- 30 X. Zhou, R. Liu, K. Sun, Y. Chen, E. Verlage, S. A. Francis, N. S. Lewis and C. Xiang, Solar-Driven Reduction of 1 atm of CO<sub>2</sub> to Formate at 10% Energy-Conversion Efficiency by Use of a TiO<sub>2</sub>-Protected III–V Tandem Photoanode in Conjunction with a Bipolar Membrane and a Pd/C Cathode, *ACS Energy Lett.*, 2016, **1**, 764–770.
- 31 D. A. Vermaas and W. A. Smith, Synergistic Electrochemical CO<sub>2</sub> Reduction and Water Oxidation with a Bipolar Membrane, *ACS Energy Lett.*, 2016, **1**, 1143–1148.
- 32 M. B. McDonald, S. Ardo, N. S. Lewis and M. S. Freund, Use of Bipolar Membranes for Maintaining Steady-State pH Gradients in Membrane-Supported, Solar-Driven Water Splitting, *ChemSusChem*, 2014, **7**, 3021–3027.
- 33 N. S. Lewis, Developing a scalable artificial photosynthesis technology through nanomaterials by design, *Nat. Nanotechnol.*, 2016, **11**, 1010–1019.
- 34 M. Nazemi, J. Padgett and M. C. Hatzell, Acid/Base Multi-Ion Exchange Membrane-Based Electrolysis System for Water Splitting, *Energy Technol.*, 2017, **5**, 1191–1194.
- 35 F. Urbain, P. Tang, N. M. Carretero, T. Andreu, L. G. Gerling, C. Voz, J. Arbiol and J. R. Morante, A prototype reactor for highly selective solar-driven CO<sub>2</sub> reduction to synthesis gas using nanosized earth-abundant catalysts and silicon photovoltaics, *Energy Environ. Sci.*, 2017, **10**, 2256–2266.

- 36 M. Manohar, G. Shukla, R. P. Pandey and V. K. Shahi, Efficient bipolar membrane with protein interfacial layer for optimal water splitting, *J. Ind. Eng. Chem.*, 2017, **47**, 141–149.
- 37 M. B. McDonald and M. S. Freund, Graphene Oxide as a Water Dissociation Catalyst in the Bipolar Membrane Interfacial Layer, *ACS Appl. Mater. Interfaces*, 2014, **6**, 13790–13797.
- 38 M.-S. Kang, Y.-J. Choi and S.-H. Moon, Effects of inorganic substances on water splitting in ion-exchange membranes: II. Optimal contents of inorganic substances in preparing bipolar membranes, *J. Colloid Interface Sci.*, 2004, **273**, 533–539.
- 39 C. Shen, R. Wycisk and P. N. Pintauro, High performance electrospun bipolar membrane with a 3D junction, *Energy Environ. Sci.*, 2017, **10**, 1435–1442.
- 40 S. Abdu, K. Sricharoen, J. E. Wong, E. S. Muljadi, T. Melin and M. Wessling, Catalytic Polyelectrolyte Multilayers at the Bipolar Membrane Interface, *ACS Appl. Mater. Interfaces*, 2013, **5**, 10445–10455.
- 41 R. Fu, T. Xu, G. Wang, W. Yang and Z. Pan, PEG-catalytic water splitting in the interface of a bipolar membrane, *J. Colloid Interface Sci.*, 2003, **263**, 386–390.
- 42 A. Alcaraz, P. Ramírez, S. Mafé and H. Holdik, A Simple Model for Ac Impedance Spectra in Bipolar Membranes, *J. Phys. Chem.*, 1996, **100**, 15555–15561.
- 43 S. Mafé and P. Ramírez, Electrochemical characterization of polymer ion-exchange bipolar membranes, *Acta Polym.*, 1997, **48**, 234–250.
- 44 H. D. Hurwitz and R. Dibiani, Experimental and theoretical investigations of steady and transient states in systems of ion exchange bipolar membranes, *J. Membr. Sci.*, 2004, **228**, 17–43.
- 45 V. M. Volgin and A. D. Davydov, Ionic transport through ion-exchange and bipolar membranes, *J. Membr. Sci.*, 2005, **259**, 110–121.
- 46 H. Strathmann, J. J. Krol, H.-J. Rapp and G. Eigenberger, Limiting current density and water dissociation in bipolar membranes, *J. Membr. Sci.*, 1997, **125**, 123–142.
- 47 R. Simons, Strong electric field effects on proton transfer between membrane-bound amines and water, *Nature*, 1979, **280**, 824–826.
- 48 R. Simons and G. Khanarian, Water dissociation in bipolar membranes: Experiments and theory, *J. Membr. Biol.*, 1978, **38**, 11–30.
- 49 L. Onsager, Deviations from Ohm's Law in Weak Electrolytes, *J. Chem. Phys.*, 1934, **2**, 599–615.
- 50 A. Alcaraz, P. Ramírez, J. A. Manzanares and S. Mafé, Conductive and Capacitive Properties of the Bipolar Membrane Junction Studied by AC Impedance Spectroscopy, *J. Phys. Chem. B*, 2001, **105**, 11669–11677.
- 51 S. Mafé, P. Ramírez and A. Alcaraz, Electric field-assisted proton transfer and water dissociation at the junction of a fixed-charge bipolar membrane, *Chem. Phys. Lett.*, 1998, **294**, 406–412.
- 52 H. Holdik, A. Alcaraz, P. Ramírez and S. Mafé, Electric field enhanced water dissociation at the bipolar membrane junction from ac impedance spectra measurements, *J. Electroanal. Chem.*, 1998, **442**, 13–18.
- 53 S. Mafé, J. A. Manzanares and P. Ramirez, Model for ion transport in bipolar membranes, *Phys. Rev. A: At., Mol., Opt. Phys.*, 1990, **42**, 6245–6248.
- 54 L. Zhu, J. Pan, C. M. Christensen, B. Lin and M. A. Hickner, Functionalization of Poly(2,6-dimethyl-1,4-phenylene oxide)s with Hindered Fluorene Side Chains for Anion Exchange Membranes, *Macromolecules*, 2016, **49**, 3300–3309.
- 55 L. Zhu, T. J. Zimudzi, Y. Wang, X. Yu, J. Pan, J. Han, D. I. Kushner, L. Zhuang and M. A. Hickner, Mechanically Robust Anion Exchange Membranes via Long Hydrophilic Cross-Linkers, *Macromolecules*, 2017, **50**, 2329–2337.
- 56 L. Zhu, J. Pan, Y. Wang, J. Han, L. Zhuang and M. A. Hickner, Multication Side Chain Anion Exchange Membranes, *Macromolecules*, 2016, **49**, 815–824.
- 57 S. Chabi, A. G. Wright, S. Holdcroft and M. S. Freund, Transparent Bipolar Membrane for Water Splitting Applications, *ACS Appl. Mater. Interfaces*, 2017, **9**, 26749–26755.
- 58 M. B. McDonald, M. Freund and P. T. Hammond, Catalytic, Conductive Bipolar Membrane Interfaces via Layer-by-Layer Deposition for the Design of Membrane-Integrated Artificial Photosynthesis Systems, *ChemSusChem*, 2017, **10**, 4599–4609.
- 59 H.-L. Lin, T. L. Yu, C.-H. Huang and T.-L. Lin, Morphology study of Nafion membranes prepared by solutions casting, *J. Polym. Sci., Part B: Polym. Phys.*, 2005, **43**, 3044–3057.
- 60 C. Welch, A. Labouriau, R. Hjelm, B. Orler, C. Johnston and Y. S. Kim, Nafion in Dilute Solvent Systems: Dispersion or Solution?, *ACS Macro Lett.*, 2012, **1**, 1403–1407.
- 61 D. T. Conroy, R. V. Craster, O. K. Matar, L.-J. Cheng and H.-C. Chang, Nonequilibrium hysteresis and Wien effect water dissociation at a bipolar membrane, *Phys. Rev. E: Stat., Nonlinear, Soft Matter Phys.*, 2012, **86**, 056104.
- 62 J. M. Ahlfield, L. Liu and P. A. Kohl, PEM/AEM Junction Design for Bipolar Membrane Fuel Cells, *J. Electrochem. Soc.*, 2017, **164**, F1165–F1171.
- 63 T. Sokalski, P. Lingenfelter and A. Lewenstam, Numerical Solution of the Coupled Nernst-Planck and Poisson Equations for Liquid Junction and Ion Selective Membrane Potentials, *J. Phys. Chem. B*, 2003, **107**, 2443–2452.
- 64 J. Leibovitz, Theorems of Electrochemical Mass Transport in Dilute Solutions of Mixtures of Electrolytes, Including Weak Electrolytes and Hydrolysis Reactions, *J. Electrochem. Soc.*, 2005, **152**, E282–E297.
- 65 R. Femmer, A. Mani and M. Wessling, Ion transport through electrolyte/polyelectrolyte multi-layers, *Sci. Rep.*, 2015, **5**, srep11583.
- 66 M. Ünlü, J. Zhou and P. A. Kohl, Hybrid Anion and Proton Exchange Membrane Fuel Cells, *J. Phys. Chem. C*, 2009, **113**, 11416–11423.
- 67 K. N. Grew, J. P. McClure, D. Chu, P. A. Kohl and J. M. Ahlfield, Understanding Transport at the Acid-Alkaline Interface of Bipolar Membranes, *J. Electrochem. Soc.*, 2016, **163**, F1572–F1587.